Thermal Conductivity of Nanocrystalline Silicon: Importance of Grain Size and Frequency-Dependent Mean Free Paths

Zhaojie Wang,[†] Joseph E. Alaniz,[†] Wanyoung Jang,[†] Javier E. Garay,[†,‡] and Chris Dames[*,†,‡]

[†]Department of Mechanical Engineering and [‡]Program in Materials Science and Engineering, University of California, Riverside, California 92521, United States

S Supporting Information

ABSTRACT: The thermal conductivity reduction due to grain boundary scattering is widely interpreted using a scattering length assumed equal to the grain size and independent of the phonon frequency (gray). To assess these assumptions and decouple the contributions of porosity and grain size, five samples of undoped nanocrystalline silicon have been measured with average grain sizes ranging from 550 to 64 nm and porosities from 17% to less than 1%, at temperatures from 310 to 16 K. The samples were prepared using current activated, pressure assisted densification (CAPAD). At low temperature the thermal conductivities of all samples show a T^2 dependence which cannot be explained by any traditional gray model. The measurements are explained over the entire temperature range by a new frequency-dependent model in which the mean free path for grain boundary scattering is inversely proportional to the phonon frequency, which is shown to be consistent with asymptotic analysis of atomistic simulations from the literature. In all cases the recommended boundary scattering length is smaller than the average grain size. These results should prove useful for the integration of nanocrystalline materials in devices such as advanced thermoelectrics.

KEYWORDS: Spark plasma sintering (SPS), thermal conductivity, nanograin, grain boundary scattering, thermoelectric
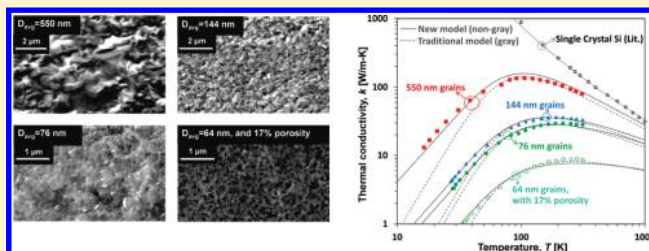
Nanocrystalline materials are promising for many applications because they provide a low-cost, bulk scale synthesis route to realize the performance advantages of nanostructuring. Potential applications include a wide range of functional and structural materials such as magnetic materials with high exchange bias,[1] optical switches and lasers,[2] and materials with improved mechanical strength and fracture toughness.[3] Of particular recent interest are high-performance, low-cost thermoelectric (TE) materials for refrigeration and energy scavenging. In nanocrystalline TE materials it has recently been shown[4−7] that the thermal conductivity k can be decreased while preserving the electronic power factor, thus increasing the figure of merit ZT in nanocrystalline materials at much lower cost than in epitaxially grown superlattices.

The dominant mechanisms for thermal conductivity reduction in nanocrystalline materials are the effects of porosity and phonon scattering at grain boundaries. However, a quantitative understanding of these two mechanisms has been lacking, because of the challenges in isolating these effects from each other and from other phonon scattering mechanisms including phonon−phonon (umklapp) scattering and impurity/alloy scattering. Grain boundary scattering coupled with other scattering mechanisms has been studied experimentally in a wide variety of materials. Early studies by Goldsmid, Parrot, Rowe, and coworkers showed significant reductions of the thermal conductivity of heavily doped TE alloys with micrometer-sized grains.[8−10] Recent measurements on nanocrystalline TE materials including Si,[6] SiGe,[7,11] and Bi$_x$Sb$_{2−x}$Te$_3$[4,5] showed even larger reductions, by up to 90%.[6] Non-TE materials have yielded similar effects, including reductions by 60−90% in micrometer-grained Y$_3$A$_5$O$_{12}$ (ref 12) and nanocrystalline yttria-stabilized zirconia.[13]

The physics of thermal conductivity is commonly interpreted using kinetic theory

$$k = \frac{1}{3} \sum_{\text{pol}} \int C v \Lambda_{\text{eff}} \, d\omega \qquad (1)$$

where C is the spectral heat capacity, v is the group velocity, ω is the frequency, Λ_{eff} is the effective mean free path (MFP), and the sum runs over all phonon polarizations. Λ_{eff} includes all those scattering mechanisms present in a bulk sample, Λ_{bulk}, as well as additional scattering due to grain boundaries, Λ_{bdy}, which are combined using Matthiessen's rule: $\Lambda_{\text{eff}}^{-1} = \Lambda_{\text{bulk}}^{-1} + \Lambda_{\text{bdy}}^{-1}$.

The greatest challenge in quantitatively predicting this thermal conductivity reduction is in calculating the effective MFP for grain boundary scattering

$$\Lambda_{\text{bdy}} = f(D_{\text{avg}}, \omega) \qquad (2)$$

Here Λ_{bdy} is a function of the average grain size, D_{avg}, and phonon frequency. In general eq 2 may also depend on atomistic

Table 1. The Processing Conditions, Densities, and Average Grain Sizes of the Samples Used in This Study

sample code D_{avg} (ρ%)	processing temperature (°C)	hold time (min)	density, ρ (% of pure Si)	average grain size, D_{avg} (nm)	std dev of distribution, (% of D_{avg})
550 (99%)	≈1250	1	99.5	550	48
144 (99%)	≈1250	2.5	99.4	144	28
76 (99%)	1200	2.27	99.1	76	30
80 (97%)	1190	0	96.7	80	26
64 (83%)	1054	0	83.0	64	35

details such as the grain boundary structure, impurity atoms at the boundary, etc., which affect the phonon transmission and reflection at each interface,[14−18] and have been predicted by Klemens[19] to give a frequency dependence $\Lambda_{bdy} \propto D_{avg}\omega^n$ with n ranging from 0 to −2. However, by far the most common approach[6−9,11,13,20,21] to eq 2 treats Λ_{bdy} as "gray" (independent of ω) and simply equates the two length scales

$$\Lambda_{bdy} \approx D_{avg} \tag{3}$$

Although eq 3 is widely used and is a plausible first-order estimate for Λ_{bdy}, it has not been justified by direct comparison with experiments on a well-understood model system. Thus, the primary goal of the present work is to experimentally quantify the effects of grain size and porosity on the phonon thermal conductivtiy of nanocrystalline materials. We focus here on undoped silicon because most previous applications of eq 3 were for systems complicated by multiple other phonon scattering mechanisms[6−9,11,13,20,21] such as alloy atoms and ionized dopants, and in some cases porosity of several percent or more, all of which complicate a direct assessment of the grain boundary scattering itself.

Experimental Details. *A. Sample Preparation.* The samples used in this study were prepared using current activated, pressure assisted densification (CAPAD), also known as spark plasma sintering (SPS) or the field assisted sintering technique (FAST).[22] This method uses large current densities (typically around 2000 A applied to a sample 19 mm in diameter and 1 mm thick) to induce rapid joule heating while simultaneously applying high pressure (typically 106 MPa) to the material. Compared to conventional hot pressing, the CAPAD technique requires much less processing time, thereby minimizing undesired grain coarsening while still resulting in sample densities exceeding 99% of the theoretical full density.

The starting material for four out of five samples was approximately 1 g of silicon powder with an average grain size of ≤50 nm and a typical agglomerate size of 10−15 μm. The fifth sample, with the largest final grain size after processing, was made from 1 g of a coarse powder with an agglomerate size of −100 + 325 mesh (approximately 44−150 μm); note that the grain size of this latter powder is much smaller than that suggested by the mesh size, because the grains were always found to be joined into large agglomerates.

Because these starting powders were exposed to the atmosphere, we expect that they have a native SiO_2 layer of thickness around 1 nm[23] on the outermost surface of each agglomerate. Approximating a typical agglomerate as a sphere of 10 μm diameter, we estimate an SiO_2 concentration on a volumetric basis of ~0.06%. To check for oxygen and other possible impurities, both starting powders and several samples produced from each powder were analyzed with X-ray diffraction (XRD) and energy-dispersive X-ray spectroscopy (EDS) spot checks, with no impurities observed above the detection threshold (approximately 5 atom % for XRD and 0.5 atom % for EDS).

The CAPAD apparatus used in this work has been described previously[22] so here we give only a few key details. The inside of the die and the ends of both plungers were wrapped in graphite paper to prevent fusion to the samples. Each sample was cold-pressed at 70.5 MPa for approximately 1 min and the processing chamber was evacuated below 1.0×10^{-2} Torr prior to the application of any current. Direct current was then applied gradually to increase the temperature at approximately 200 °C/min to the target temperatures given in Table 1, requiring typically 1600−1900 A. For the three densest samples the target temperature was held for one or more minutes. For all five samples the current ramp was accompanied by a simultaneous pressure ramp at 35.3 MPa/min to the maximum pressure of 106 MPa.

Table 1 summarizes selected processing conditions used to control grain size and porosity. The first column gives a code for each sample, of the form $D_{avg}(\rho\%)$, where D_{avg} is in nanometers and ρ is the density normalized to that of pure single crystal (bulk) silicon. The second column gives the processing temperature. Temperatures above 1200 °C are approximate because those experiments were current-controlled rather than temperature-controlled, due to limitations of the thermocouple used. As expected, samples processed at higher temperature and longer hold times have larger average grain sizes and higher densities due to thermally activated grain growth and densification. The first three samples in Table 1 were designed to span a large range of grain size while maintaining very high density ($\rho > 99\%$), while the fourth and fifth samples were designed to have similar small grain sizes as the third sample but with significantly lower densities ($\rho \leq 97\%$).

B. Sample Characterization. Figure 1 shows scanning electron microscopy (SEM) micrographs of fracture surfaces on samples 550 (99%), 144 (99%), and 76 (99%) and polished surfaces on samples 80 (97%) and 64 (83%). Note the prominent porosity in the last two samples while no porosity is evident for the first three samples. The grains are approximately equiaxed. For each sample, the diameters of approximately 200 distinct grains were measured from an SEM image of a fracture surface. As detailed in the Supporting Information, for each sample the measured distribution of grain sizes is approximately log-normal, with D_{avg} and standard deviation given in Table 1.

After residual carbon was removed from the graphite paper by polishing, the density of the samples was measured using an Archimedes method. Because the pores are not connected, the water does not penetrate the samples. The Archimedes method should be more accurate than using volume measured by caliper measurements, because the latter are subject to errors if there are any irregularities in the sample shape.
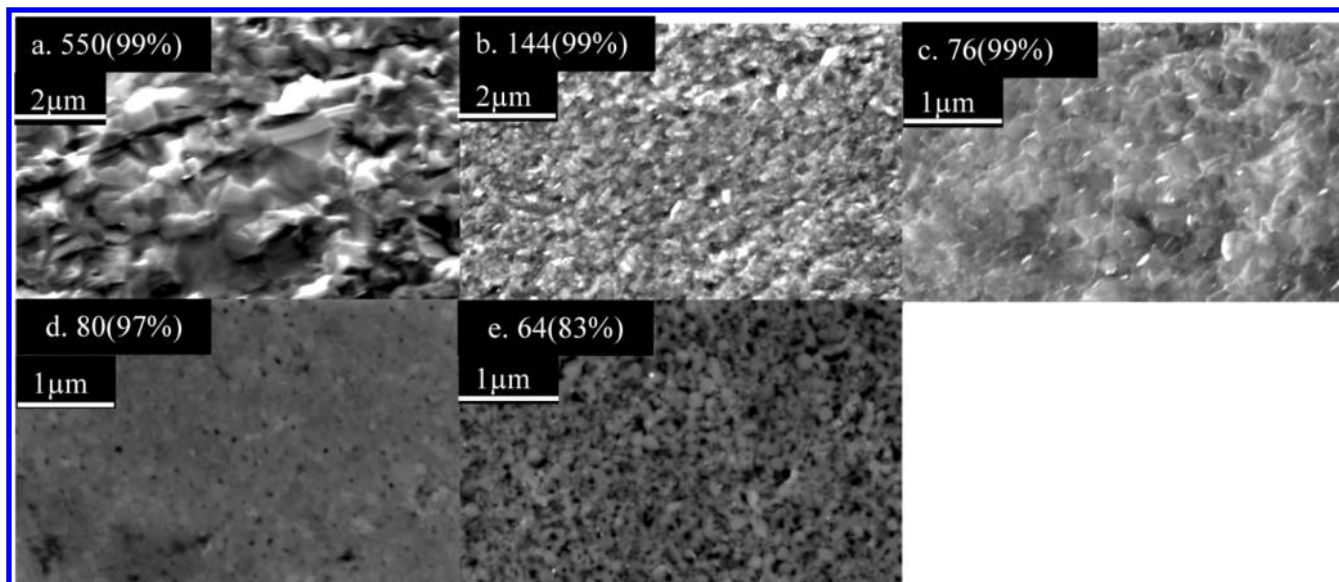
Figure 1. SEM micrographs of the samples used in this study. (a−c) are fracture surfaces, while (d) and (e) are polished surfaces to facilitate clear visualization of the pores.

C. Thermal Conductivity Measurements. We measure the thermal conductivity using a standard 3ω method.[24,25] Although these samples are expected to be electrically insulating because the starting powders are undoped, as was checked on several samples by probing with a multimeter, to further ensure electrical insulation all samples are polished and then spin-coated with 110 nm of dielectric hydrogen-silsesquioxane (HSQ: FOx from Dow Corning) prior to microfabrication. Then a gold heater line is patterned by photolithography and a liftoff method. The heater line is 10 μm wide, 250 nm thick, and spans 1 mm between the inner voltage probes.

The standard 3ω method uses the continuum heat diffusion equation for data analysis to obtain the effective k of the nanocrystalline substrate. To justify this continuum approximation it is important to verify that the phonon MFPs are significantly smaller than the heater line width w_H at all temperatures. As detailed in the Supporting Information, following ref 32 we calculated the distributions of MFPs that contribute to k in these samples. For both models of Λ_{Bdy} presented in the Discussion Section below, the calculations show that the important MFPs are indeed much smaller than w_H for the four samples with $D_{avg} \leq 144$ nm at all temperatures of interest, making the continuum 3ω analysis an excellent approximation. For the largest-grained sample with $D_{avg} = 550$ nm, the calculations also verify that the important MFPs are also much smaller than w_H for T as low as ∼30 K, although in the frequency-dependent model of Λ_{Bdy} below 30 K a small fraction of the heat is carried by MFPs larger than w_H. We have also confirmed that the thermal diffusion wavelength ($\lambda_{diff} = (\kappa/4\pi f_H)^{1/2}$, where κ is the thermal diffusivity and f_H is the heater frequency, typically 100−1000 Hz) in these experiments is much larger than D_{avg} and w_H, as required for standard 3ω analysis.

Because these measurements extend well below 50 K, the nonlinearity of the resistance versus temperature calibration $R(T)$ of the gold heater line is an important detail. We use an analytical Bloch−Gruneisen function[26,27] to fit the $R(T)$ calibration data for every sample, which is then differentiated analytically. Another detail is that the temperature of the gold heater line
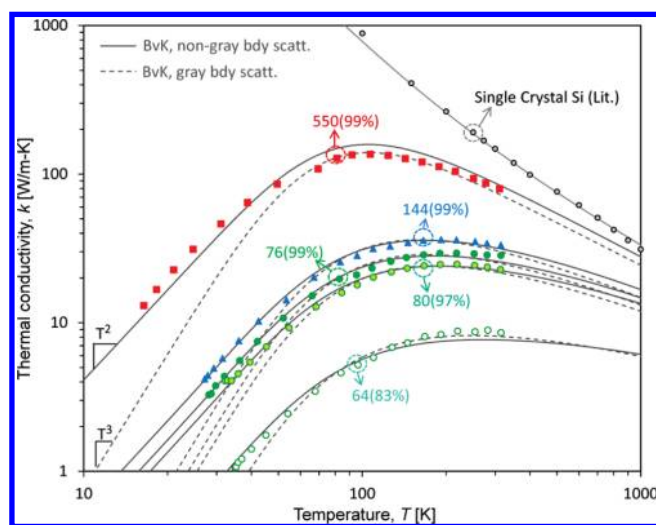
Figure 2. Measured (points) and modeled (lines) thermal conductivity for nanocrystalline silicon. Measurements for single-crystal Si are from TPRC.[29] The lines are fits using a Born−von Karman (BvK) dispersion relation and include both gray (dashed lines, eq 6) and frequency-dependent (solid lines, eq 7) expressions for grain boundary scattering, using the characteristic lengths given in Figure 3a. At low temperatures only the frequency-dependent model captures the T^2 trend evident in the experiments.

and adjacent silicon can be significantly higher than that of the cryostat's coldfinger, particularly at low T. Therefore, for every data point we monitor the average value of the heater line's resistance and use its $R(T)$ calibration to determine its temperature, which is then used as a better indicator of the temperature of the silicon immediately beneath the heater. The small temperature drop through the HSQ layer has been neglected because we estimate it contributes less than 5% error in the assigned temperature.[28]

Experimental Results. Figure 2 shows the complete experimental results for the five nanocrystalline Si samples measured in
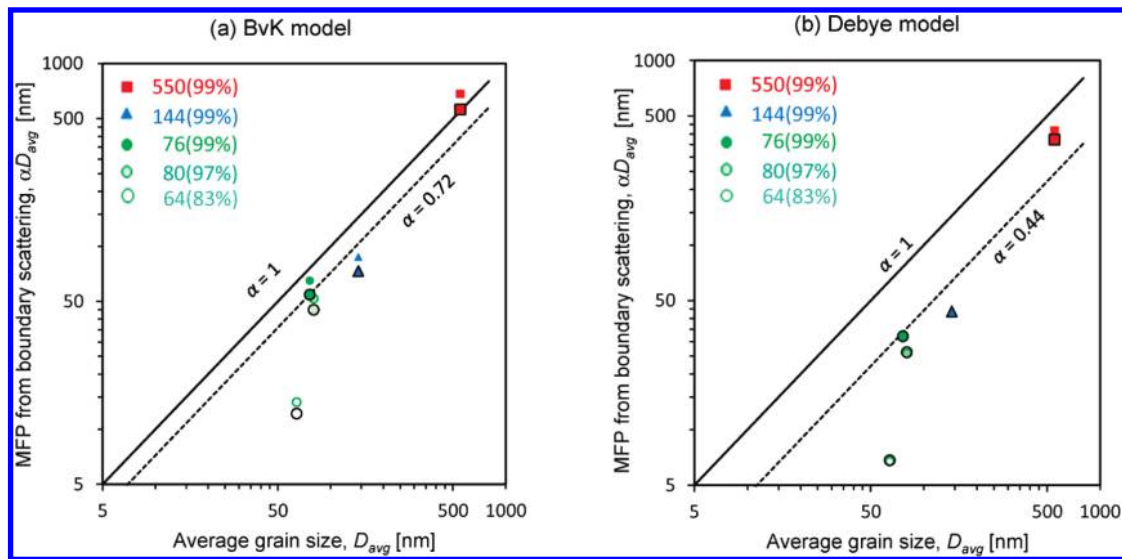
Figure 3. Best-fit values of the characteristic MFPs for boundary scattering as a function of average grain size for models using either (a) Born–von Karman or (b) Debye phonon dispersion. The larger points with black borders are for frequency-dependent grain boundary scattering, obtained by fitting Figure 2 with eq 7 for all T, while the smaller points are for gray grain boundary scattering, obtained by fitting Figure 2 with eq 6 for $T > 64$ K. For the Debye model these two sets of points are almost indistinguishable.

this study. The modeling curves and Figure 3 will be explained shortly. The nanocrystalline samples' k is always smaller than that of single crystal Si,[29] most dramatically at lower T and for smaller-grained samples with lower density. By comparison with the single crystal data, it is clear that most of the measurements in this work are in the ballistic regime where the phonon scattering is dominated by grain boundaries and porosity effects. Umklapp scattering is also important in the larger-grained samples near room temperature, as is apparent from the negative slope in the $k(T)$ curves.

All five samples in Figure 2 show an unexpected power law of $k \propto T^2$ at low temperature, in marked contrast to the T^3 power law that is typically seen in bulk single crystals,[29] nanowires,[30] and thin films.[31] From the kinetic theory expression of eq 1, it is well-known that the familiar $k \propto T^3$ trend arises from the T^3 specific heat well below the Debye temperature T_{Debye}, combined with strong boundary scattering that is independent of frequency (gray). Referring to eq 1, we consider two possible explanations of the T^2 trend of Figure 2: an altered dispersion relation affecting C and v or frequency-dependent boundary scattering affecting Λ_{eff}.

We first consider the possible effect of the small grain sizes on the dispersion relation and C and v, which are expected to be significantly changed if the important phonon wavelengths λ are comparable to D_{avg}.[33] However, as described in the Supporting Information (see also ref 32) the range of important λ contributing to heat transfer is calculated to be ∼10 nm or smaller even at the lowest temperatures of this study. Because these wavelengths are much smaller than D_{avg}, and considering that the variations in D of any given sample are comparable to if not much larger than λ, we expect that confinement effects on the phonon dispersion can be neglected to an excellent approximation. Therefore, we conclude that the phonon dispersion in these samples should be well-approximated by the bulk (three-dimensional) phonon dispersion with $C \propto T^3$ at low T (ref 33) and conclude that the Cv term of eq 1 cannot explain the T^2 trend of Figure 2.

However, the T^2 trend of Figure 2 can be explained by allowing Λ_{bdy} to have a frequency dependence (nongray). A detailed

model appropriate for all T is given in the Discussion Section below. Here consider briefly the low-T limit of a Debye model with strong boundary scattering, in which case it is well-known[34] that eq 1 simplifies to

$$ k = \frac{k_B v_s}{2\pi^2} \left(\frac{k_B T}{\hbar v_s} \right)^3 \int_0^\infty \frac{x^4 e^x \Lambda_{bdy}}{(e^x - 1)^2} \, dx \qquad (4) $$

where k_B is the Boltzmann constant, $\hbar$ is the reduced Planck's constant, v_s is a triply degenerate averaged sound velocity, and $x = \hbar\omega/k_B T$. In this limit it is easily shown analytically that if $\Lambda_{bdy} \propto \omega^n$, then $k \propto T^{3+n}$. Thus, the low-T trend of $k \propto T^2$ strongly suggests $\Lambda_{bdy} \propto \omega^{-1}$ for small ω, which is within the range $-2 \leq n \leq 0$ suggested by Klemens,[19] and as discussed below is also consistent with several atomistic simulations of frequency-dependent interfacial scattering from the literature. Thus, surprisingly, the widespread assumption of gray grain boundary scattering[6−9,11,13,20,21] indicated by the dashed lines in Figure 2 is not a good approximation for these measurements below about 70 K. An improved model is given in the Discussion Section below.

To highlight the effect of grain size, Figure 4 shows k as a function of D_{avg} for the fully dense samples ($\rho > 99\%$) at three temperatures. The experimental points are obtained by power law interpolation from the main data set of Figure 2, and the modeling curves will be explained shortly. At low T the power law is $k \propto D^1$, as expected for a system dominated by boundary scattering, while for higher T and larger grains the $k(D)$ power law becomes weaker due to the increasing importance of umklapp scattering.

Figure 5 shows the porosity dependence of the thermal conductivity for the three samples that have approximately the same average grain size (within ±11% of 72 nm). To facilitate comparisons, for each temperature, the k values in Figure 5 are normalized to the k values of the almost-fully dense sample, 76 (99%). Three classical models for porous media based on Fourier's law are also shown.[35−37] These classical theories are most appropriate for isolated pores that are approximately spherical,
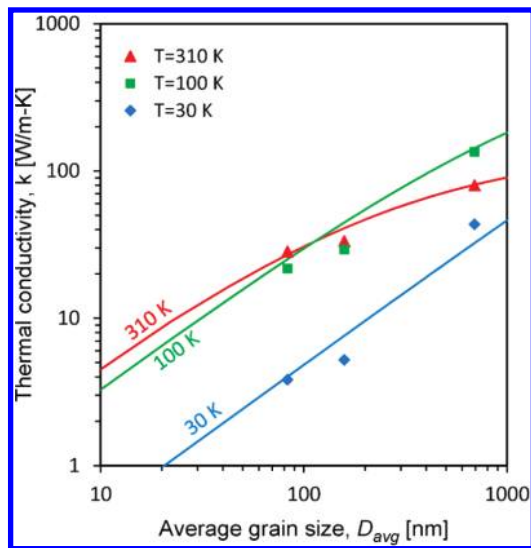
Figure 4. Thermal conductivity vs average grain size for fully dense samples 550 (99%), 144 (99%), and 76 (99%) at three temperatures. The model (lines) uses the nongray BvK model with $\alpha = 0.72$.
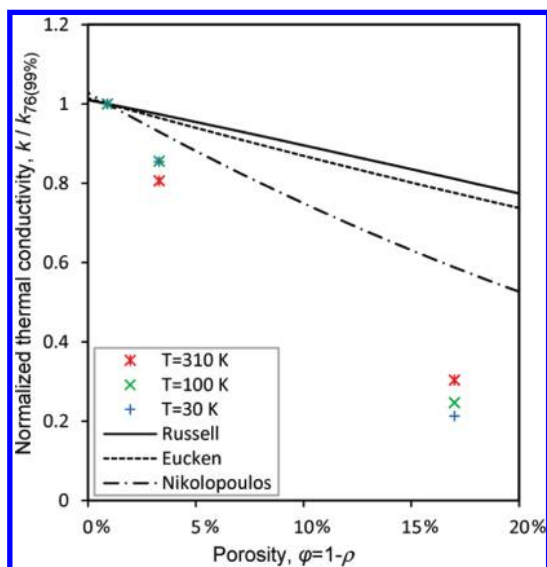
Figure 5. Normalized thermal conductivity vs porosity for the fine-grained samples 76 (99%), 80 (97%), and 64 (83%) at three temperatures, compared with traditional models for porous media.[35−37]

which as shown in panels d and e of Figure 1 is a good assumption for sample 80 (97%) but less so for sample 64 (83%).

It is clear that the porosity effect in these measurements is stronger than any of the classical theories. Although the slightly nonspherical pore shapes may result in a minor additional reduction in k,[38] we believe that ballistic effects are more important. Classical theories are based on diffusive transport and thus require pore sizes much larger than the phonon MFPs, which in these nanocrystalline samples are comparable to D_{avg}. However, it is clear from panels d and e of Figure 1 that the actual pore sizes are comparable to and often smaller than the grain size, so these samples violate the diffusive assumption in the neighborhood of each pore, most dramatically for sample 64 (83%) which has nearly as many pores as grains.

Table 2. The Best Fit Parameters A_1, B_1, and B_2 for Debye and BvK models, Obtained by Fitting Literature Data[29] for Single Crystal Si

model	max. frequency, $2\pi\omega_0$ (THz)	v_s (m/s)	A_1 (10^{-45} s^3)	B_1 (10^{-19} s/K)	B_2 (K)
Debye	11.03	6084	1.81	2.69	167
BvK	7.02	6084	1.69	1.53	140

Discussion. *A. Model of Bulk Thermal Conductivity.* We interpret the measurements of Figure 2 with the kinetic theory expression of eq 1. For simplicity we neglect heat transfer by the optical phonon branches, which has been shown to be a good approximation for Si,[39] and lump the three acoustic branches into one triply degenerate branch. Our primary model uses a Born−von Karman (BvK) dispersion relation identical to that of ref 40. For comparison purposes, we also present selected results obtained using a Debye dispersion relation with the same sound velocity, v_s, and cutoff wavevector, q_0, as the BvK model. The Debye dispersion relation is widely used because of its simplicity,[6,8,9,11,12,21,31] but it is also known to significantly overestimate the group velocity of high-energy phonons, thereby underestimating the bulk MFPs obtained by fitting and thus missing out on the full reduction in k for nanostructures of moderate size.[32,40]

The phonon scattering mechanisms include impurity/defect scattering Λ_{imp}, umklapp scattering Λ_{umkl}, and grain boundary scattering Λ_{bdy}, combined using Matthiessen's rule

$$\Lambda_{eff}^{-1}(\omega, T) = \Lambda_{imp}^{-1}(\omega) + \Lambda_{umkl}^{-1}(\omega, T) + \Lambda_{bdy}^{-1}(\omega) \quad (5)$$

For impurity scattering we use a Rayleigh-like expression, $\Lambda_{imp}^{-1} = A_1\omega^4/v$, and for umklapp scattering we use one common form,[41] $\Lambda_{umkl}^{-1} = B_1\omega^2 Te^{(-B_2/T)}/v$. We determine the parameters A_1, B_1, and B_2 for the BvK and Debye models separately (Table 2) by fitting each model to literature data for single crystal silicon.[29] The high-temperature portion of the fit for the BvK model is apparent in Figure 2.

B. Gray Model for Grain Boundary Scattering. As noted in eq 3, the most widespread model of grain boundary scattering is gray, with $\Lambda_{bdy} = D_{avg}$. As an initial generalization we consider

$$\Lambda_{bdy} = \alpha D_{avg} \quad (6)$$

where the parameter α is introduced to account for the effect of grain boundary transmission: for lower transmission coefficients we expect smaller α and thus smaller k. Because all gray models fail to capture the T^2 trend seen in the experiments at low temperature, we fit eq 6 to Figure 2 only for $T > 64$ K. Details of the fitting process are given in the Supporting Information. The resulting best-fit model curves are shown by the dashed lines in Figure 2, and the corresponding α values shown by the smaller points in Figure 3. It is clear that even above 64 K the simple expression $\Lambda_{bdy} = D_{avg}$ (solid line in Figure 3) is not the best description of these measurements. Instead, eq 6 with $\alpha < 1$ is a better description. Thus, for either dispersion model we find that the effective MFPs for grain boundary scattering are smaller than those implied by the widely used assumption $\alpha = 1$.

C. Frequency-Dependent (Nongray) Model for Grain Boundary Scattering. We now return to the T^2 trend seen in Figure 2 at low T, which as discussed above and further justified below strongly suggests $\Lambda_{bdy} \propto \omega^{-1}$ for small ω. Although the full behavior of $\Lambda_{bdy}(D_{avg}, \omega)$ for all ω is unknown and is likely to be

Table 3. Recommended Values of α for Fully Dense Samples Using Four Different Models

	BvK dispersion	Debye dispersion
nongray Λ_{bdy}, eq 7 (recommended for all T)	0.72	0.44
Gray Λ_{bdy}, eq 6 (may be acceptable for $T > 80$ K if other scattering mechanisms can be neglected; see Supporting Information)	0.86	0.47

a complicated function of ω, here we hypothesize that the ω^{-1} power law is an adequate approximation over all frequencies, and thus generalize eq 6 as

$$\Lambda_{bdy} = \alpha D_{avg}(\beta\omega_0/\omega) \qquad (7)$$

Equation 7 introduces a numerical constant β which, like ω_0, depends on the choice of dispersion relation used in the model. We emphasize that β is not a fitting parameter but rather is fixed analytically by requiring eq 7 to give the same value of α as the gray model of eq 6, in the limit of strong boundary scattering and $T \gg T_{Debye}$. As detailed in the Supporting Information, in this limit we find $\beta = 2/3$ for a Debye dispersion and

$$\beta = \frac{16 - 2\pi^2}{7\zeta(3) - 2\pi^2 \ln(2)} = 0.7097$$

for a BvK dispersion, where ζ is the Riemann zeta function. Recognizing that there is little difference between these two values and considering that most real acoustic phonon branches should be bounded by the Debye and BvK approximations, for most purposes the value $\beta = 0.70$ should suffice.

D. Comparison of Various Models. The solid lines in Figure 2 show the results of fitting our experimental data with the frequency-dependent grain boundary scattering law of eq 7 and a BvK dispersion. The five corresponding values of α are shown by the larger set of points in Figure 3a. For fully dense samples, the recommended values of α for the four models considered are summarized in Table 3. The α values for a Debye model are smaller than the α values for a BvK model primarily because the former overpredicts the average group velocity as compared to the latter.

On comparison of the solid and dashed lines in Figure 2, it is clear that these measurements are described much better by the new frequency-dependent model of eq 7 than the standard gray approach of eq 6. A more quantitative comparison is given in the Supporting Information, which shows that a BvK dispersion outperforms a Debye dispersion regardless of the chosen model for Λ_{bdy}, and similarly that the frequency-dependent Λ_{bdy} is better than the gray Λ_{bdy} regardless of the chosen dispersion relation. Averaged across the five samples, the root-mean-square (rms) residual for a model using the BvK dispersion and nongray Λ_{bdy} is only 7%. In contrast, for the most common approach using the Debye dispersion and gray Λ_{bdy}, the average residuals are significantly worse, at 77%.

E. Atomistic Interpretation. We now give an atomistic interpretation of the $\Lambda_{bdy} \propto \omega^{-1}$ frequency dependence of eq 7. At the scale of individual grains, the MFP for boundary scattering is determined by D and the specularity and transmissivity of phonons at each grain boundary. For example, for reflections by boundaries parallel to the heat current, Ziman[42,43] derived

a frequency-dependent expression for specularity, $p = \exp[-(16\pi^2\eta^2)/\lambda^2]$, where η is the rms surface roughness.[44] Similarly, heat transfer perpendicular to an interface can be described by $t(\omega)$, the phonon transmissivity, which has been modeled for idealized interfaces using Green's functions,[14] molecular dynamics,[15,16,45] and acoustic and diffuse mismatch models.[12,46]

However, even if the $p(\omega)$ and $t(\omega)$ functions are assumed known for the boundaries of interest, calculating the corresponding Λ_{bdy} is still a challenge. Klemens[19] argued that Λ_{bdy} should scale as $D_{avg}\omega^n$ with $-2 \leq n \leq 0$, with a prefactor that depends on the angle and density of dislocations at the grain boundary and various material properties. Another approach uses molecular dynamics simulations combined with finite element methods,[45] though this lacks an analytical form. Here we introduce a simple analytical framework. The polycrystal is approximated as a superlattice nanowire, which incorporates the effects of scattering by boundaries both parallel to and perpendicular to the transport direction, ultimately leading to[40]

$$\Lambda_{bdy}^{-1} = \left[\left(\frac{\frac{3}{4}t(\omega)}{1 - t(\omega)} \right)^{-1} + \left(\frac{1 + p(\omega)}{1 - p(\omega)} \right)^{-1} \right] D_{avg}^{-1} \qquad (8)$$

Equation 8 yields further insight by considering the limiting behaviors of $t(\omega)$ and $p(\omega)$ effects separately. First, consider the limit where the overall transport is limited by the transmissivity. We expect this limit to be most relevant because high-quality grain boundaries should be smooth and have large p (ref 42) and also because a separate analysis[47] of the effective k of a nanocomposite showed that the overall transport is most often limited by scattering perpendicular to interfaces (t effect) rather than parallel to interfaces (p effect). In this limit eqs 7 and 8 give

$$t = \frac{\alpha\beta}{\frac{3}{4}(\omega/\omega_0) + \alpha\beta} \qquad (9)$$

which for small ω can be linearized as

$$t \approx 1 - \frac{3}{4}\gamma\omega \qquad (10)$$

where $\gamma = (\alpha\beta\omega_0)^{-1}$. Equation 10 is consistent with various atomistic simulations[14-18] which also predict $t \approx 1$ as $\omega \rightarrow 0$ and can be roughly approximated with a slope $dt/d\omega$ that is a negative constant for $0 < \omega < (1/2)\omega_0$.

Similarly, eq 8 can also be evaluated in the opposite limit where Λ_{bdy} is dominated by specularity effects, although we expect this to be rare in real materials. This limit yields $p = (1 - \gamma\omega)/(1 + \gamma\omega)$, which, to leading order, is also linear in ω

$$p \approx 1 - 2\gamma\omega \qquad (11)$$

This trend is not consistent with Ziman's specularity equation,[42,43] which for small ω and assuming linear dispersion can be written $p \approx 1 - (2\eta\omega/v_s)^2$, that is, parabolic in ω. However, detailed atomistic simulations of specularity by Zhao and Freund[14] show specularity trends ranging from approximately $1 - p \propto \omega^2$ (as in Ziman's expression) to $1 - p \propto \omega$ (as in eq 11).

Summarizing this discussion, because various atomistic simulations of $t(\omega)$ approximately follow eq 10 for small ω, by using eq 8 we have shown that the small-ω power law $\Lambda_{bdy} \propto \omega^{-1}$

introduced empirically in eq 7 is consistent with the asymptotic behavior of atomistic calculations.

Conclusions. This work leads to two major conclusions. First, the common strategy of setting $\Lambda_{bdy} = D_{avg}$ is not the best approximation for grain boundary scattering. If a gray model is desired for simplicity, it would be more accurate to use $\Lambda_{bdy} = \alpha D_{avg}$, where recommended values of α for fully dense Si are given in Table 3 for Born—von Karman (recommended) and Debye (more common but less accurate) model dispersions. The α values can be greatly reduced for samples with significant porosity, as shown in Figures 3 and 5, and α would also be reduced for lower-quality, less-transmissive grain boundaries.

The other major result of this study is to identify an asymptotic ω^{-1} frequency dependence in the MFPs for grain boundary scattering. This frequency dependence is necessary to explain the $k \propto T^2$ trend seen in Figure 2 at low T, and we have argued that it is also consistent with most atomistic models of grain boundary transmissivity from the literature. Unlike the traditional gray model for Λ_{bdy} from eq 3, the new frequency-dependent model of eq 7 works at all temperatures measured (16—310 K), and it outperforms the gray model for both Debye and Born—von Karman dispersion relations.

■ ASSOCIATED CONTENT

Ⓢ Supporting Information. Distributions of measured grain sizes, details of model fitting, calculated distributions of the MFPs and wavelengths that are important for heat transfer, and relationship of gray and nongray models at high temperature. This material is available free of charge via the Internet at http://pubs.acs.org.

■ AUTHOR INFORMATION

Corresponding Author
*E-mail: cdames@engr.ucr.edu.

■ ACKNOWLEDGMENT

■ REFERENCES

(1) Nogués, J.; Sort, J.; Langlais, V.; Skumryev, V.; Surinach, S.; Munoz, J.; Baró, M. *Phys. Rep.* **2005**, *422* (3), 65–117.

(2) Weber, M. *Handbook of optical materials*; CRC: Boca Raton, FL, 2003.

(3) Boyce, B. L.; Shaw, M. J.; Lu, P.; Dugger, M. T. *Acta Mater.* **2010**, *58* (2), 439–448.

(4) Poudel, B.; Hao, Q.; Ma, Y.; Lan, Y.; Minnich, A.; Yu, B.; Yan, X.; Wang, D.; Muto, A.; Vashaee, D.; Chen, X.; Liu, J.; Dresselhaus, M. S.; Chen, G.; Ren, Z. *Science* **2008**, *320* (5876), 634–638.

(5) Xie, W.; Tang, X.; Yan, Y.; Zhang, Q.; Tritt, T. M. *Appl. Phys. Lett.* **2009**, *94* (10), 102111.

(6) Bux, S. K.; Blair, R. G.; Gogna, P. K.; Lee, H.; Chen, G.; Dresselhaus, M. S.; Kaner, R. B.; Fleurial, J.-P. *Adv. Funct. Mater.* **2009**, *19* (15), 2445–2452.

(7) Joshi, G.; Lee, H.; Lan, Y.; Wang, X.; Zhu, G.; Wang, D.; Gould, R. W.; Cuff, D. C.; Tang, M. Y.; Dresselhaus, M. S.; Chen, G.; Ren, Z. *Nano Lett.* **2008**, *8* (12), 4670–4674.

(8) Goldsmid, H. J.; Penn, A. W. *Phys. Lett. A* **1968**, *27* (8), 523–524.

(9) Parrott, J. E. *J. Phys. C: Solid State Phys.* **1969**, *2* (1), 147–151.

(10) Rowe, D. M.; Shukla, V. S.; Savvides, N. *Nature* **1981**, *290* (5809), 765–766.

(11) Minnich, A. J.; Lee, H.; Wang, X. W.; Joshi, G.; Dresselhaus, M. S.; Ren, Z. F.; Chen, G.; Vashaee, D. *Phys. Rev. B* **2009**, *80*, 155327.

(12) Bisson, J.-F.; Yagi, H.; Yanagitani, T.; Kaminskii, A.; Barabanenkov, Y.; Ueda, K.-I. *Opt. Rev.* **2007**, *14* (1), 1–13.

(13) Yang, H.-S.; Bai, G. R.; Thompson, L. J.; Eastman, J. A. *Acta Mater.* **2002**, *50* (9), 2309–2317.

(14) Zhao, H.; Freund, J. B. *J. Appl. Phys.* **2009**, *105* (1), 013515–9.

(15) Aubry, S.; Kimmer, C. J.; Skye, A.; Schelling, P. K. *Phys. Rev. B* **2008**, *78*, 064112.

(16) Sun, L.; Murthy, J. Y. *J. Heat Transfer* **2010**, *132* (10), 102403–9.

(17) Schelling, P. K.; Phillpot, S. R.; Keblinski, P. *J. Appl. Phys.* **2004**, *95* (11), 6082–6091.

(18) Kimmer, C.; Aubry, S.; Skye, A.; Schelling, P. K. *Phys. Rev. B* **2007**, *75* (14), 144105.

(19) Klemens, P. G. *Solid State Phys.* **1958**, *7*, 1–98.

(20) Rowe, D. M.; Shukla, V. S. *J. Appl. Phys.* **1981**, *52* (12), 7421–7426.

(21) Kang, C.; Kim, H.; Park, S.-G.; Kim, W. *Appl. Phys. Lett.* **2010**, *96* (21), 213114–3.

(22) Garay, J. E. *Annu. Rev. Mater. Res.* **2010**, *40* (1), 445–468.

(23) Morita, M.; Ohmi, T.; Hasegawa, E.; Kawakami, M.; Ohwada, M. *J. Appl. Phys.* **1990**, *68* (3), 1272–1281.

(24) Cahill, D. G. *Rev. Sci. Instrum.* **1990**, *61* (2), 802–808.

(25) Dames, C.; Chen, G. *Rev. Sci. Instrum.* **2005**, *76* (12), 124902–14.

(26) Putnam, S. A.; Cahill, D. G.; Braun, P. V.; Ge, Z.; Shimmin, R. G. *J. Appl. Phys.* **2006**, *99* (8), 084308–6.

(27) Chen, Z.; Jang, W.; Bao, W.; Lau, C. N.; Dames, C. *Appl. Phys. Lett.* **2009**, *95* (16), 161910–3.

(28) Costescu, R. M.; Bullen, A. J.; Matamis, G.; O'Hara, K. E.; Cahill, D. G. *Phys. Rev. B* **2002**, *65* (9), 094205.

(29) Purdue University, Thermophysical Properties Research Center (TPRC). *Thermophysical Properties of Matter*; Touloukian, Y. S., Ed.; IFI/Plenum: New York, 1970—1979.

(30) Li, D.; Wu, Y.; Kim, P.; Shi, L.; Yang, P.; Majumdar, A. *Appl. Phys. Lett.* **2003**, *83* (14), 2934–2936.

(31) McConnell, A. D.; Goodson, K. E. *Annu. Rev. Heat Transfer* **2005**, *14*, 129–168.

(32) Dames, C.; Chen, G. Thermal Conductivity of Nanostructured Thermoelectric Materials. In *Thermoelectrics Handbook: macro to nano*, Rowe, D. M., Ed.; CRC Press: Boca Raton, FL, 2005.

(33) Dames, C.; Poudel, B.; Wang, W. Z.; Huang, J. Y.; Ren, Z. F.; Sun, Y.; Oh, J. I.; Opeil, C.; Naughton, M. J.; Chen, G. *Appl. Phys. Lett.* **2005**, *87* (3), 031901.

(34) Kittel, C., *Introduction to Solid State Physics*, 8th ed.; Wiley: Hoboken, NJ, 2004.

(35) Eucken, A. *Forsch. Gebiete Ingenieurw* **1932**, 3.

(36) Russell, H. W. *J. Am. Ceram. Soc.* **1935**, *18* (1—12), 1–5.

(37) Nikolopoulos, P.; Ondracek, G. *J. Am. Ceram. Soc.* **1983**, *66* (4), 238–241We use the III-order lower bounds.

(38) Liu, L.-C.; Huang, M.-J. *Int. J. Therm. Sci.* **2010**, *49* (9), 1547–1554.

(39) Broido, D. A.; Malorny, M.; Birner, G.; Mingo, N.; Stewart, D. A. *Appl. Phys. Lett.* **2007**, *91* (23), 231922–3.

(40) Dames, C.; Chen, G. *J. Appl. Phys.* **2004**, *95* (2), 682–693.

(41) Han, Y.-J. *Phys. Rev. B* **1996**, *54* (13), 8977.

(42) Ziman, J. M. *Electrons and Phonons*; Clarendon Press: Oxford, 1960.

(43) Zhang, Z. *Nano/microscale heat transfer*; McGraw-Hill Professional: New York, 2007; p 274. We have confirmed the observation by Z. Zhang and H. J. Lee that the derivation given in Ziman's book[42] contained an erroneous factor of π.

(44) The term roughness is not usually used to describe grain boundaries in polycrystalline materials. Rather their structure is commonly characterized using misorientation angles, coincident lattice sites, and other models. However, since the correlations between grain boundary structure and specularity/transmissivity of phonons are not

well understood, here we adhere to the term roughness that is common in the transport literature.

(45) Crocombette, J.-P.; Gelebart, L. *J. Appl. Phys.* **2009**, *106* (8), 083520.

(46) Swartz, E. T.; Pohl, R. O. *Rev. Mod. Phys.* **1989**, *61*, 605.

(47) Yang, F.; Ikeda, T.; Snyder, G. J.; Dames, C. *J. Appl. Phys.* **2010**, *108* (3), 034310.